CrossMark

Influence of solidification on the impact of supercooled water drops onto cold surfaces

Hai Li[1] · Ilia V. Roisman[1] · Cameron Tropea[1]

Abstract This study presents an experimental investigation of the impact of a supercooled drop onto hydrophilic and superhydrophobic substrates. The aim is to better understand the process of airframe icing caused by supercooled large droplets, which has been recently identified as a severe hazard in aviation. The Weber number and Reynolds number of the impinging drop ranged from 200 to 300 and from 2600 to 5800, respectively. Drop impact, spreading, and rebound were observed using a high-speed video system. The maximum spreading diameter of an impacting drop on hydrophilic surfaces was measured. The temperature effect on this parameter was only minor for a wide range of the drop and substrate temperatures. However, ice/water mixtures emerged when both the drop and substrate temperatures were below 0 °C. Similarly, drop rebound on superhydrophobic substrates was significantly hindered by solidification when supercooled drop impacted onto substrates below the freezing point. The minimum receding diameter and the speed of ice accretion on the substrate were measured for various wall temperatures. Both parameters increased almost linearly with decreasing wall temperature, but eventually leveled off beyond a certain substrate temperature. The rate of ice formation on the substrate was significantly higher than the growth rate of free ice dendrites, implying that multiple nucleation sites were present.

✉ Ilia V. Roisman
    roisman@sla.tu-darmstadt.de

[1] Institute of Fluid Mechanics and Aerodynamics, Center
     of Smart Interfaces, Technische Universität Darmstadt,
     Alarich-Weiss-Straße 10, 64287 Darmstadt, Germany

1 Introduction

Airframe icing is a topic of vital importance in aviation industry because it is mainly concerned with the safe and efficient operation of aircraft under all weather conditions. Over the last 15 years, the role of supercooled large droplets (SLD) in aircraft icing has received increased attention (Marwitz et al. 1997; Mingione et al. 2011).

Recent meteorological investigations about icing conditions have highlighted the existence of icing cloud characteristics beyond the current certification envelope defined by the 14 CFR Part 25 Appendix C: Atmospheric Icing Conditions for Aircraft Certification, which accounts for an icing envelope characterized by water droplet diameters up to 50 μm. Meteorological investigations discovered the diameter and temperature ranges of SLD icing condition. Typical SLD icing weather includes freezing drizzle with droplets of 200–500 μm and freezing rain with droplets larger than 500 μm. According to the measurements during CFDE I and III (first and third canadian freezing drizzle experiment), which were based on 30-s measurements and included only the cases with SLD, the largest mean volume diameter (MVD) was 404 μm, while the largest droplet was 2 mm in diameter (Cober et al. 2001). In CFDE I/III conducted in North Atlantic Ocean, the detected mean temperature of SLD cloud was about −3 °C, and the minimum temperature was higher than −10 °C (Cober et al. 2001). SLD flight research study found that the freezing rain had the lowest temperature at −9 °C in Great Lakes region (Bernstein et al. 1999). Freezing drizzle observed in AIRS (alliance icing research study I and II) undertaken in Ontario and Quebec had a similar temperature, from −8 to −10 °C (Cober and Isaac 2006). The lowest temperature of SLD at −10 °C was also confirmed by Strapp et al. (1996)

with an in situ observation of over 30 years in St. John's, Newfoundland.

Solidification of a supercooled liquid can be separated into two main stages (Bauerecker et al. 2008; Jung et al. 2012; Alizadeh et al. 2012). The first stage of solidification is characterized by a sharp temperature rise resulting from rapid growth of ice dendrites, leading to a mixed phase state. The second stage is characterized by stable solidification of the liquid water phase between dendrites. Formation of ice dendrites is a result of the morphological instability of the solid/liquid interface if the liquid is at the subfreezing temperature, known as Mullins–Sekerka instability (Mullins and Sekerka 1963, 1964).

The growth rate of ice dendrites is experimentally found to be almost logarithmically proportional to the supercooling when the initial temperature of the liquid is above $-10\ ^\circ$C (Shibkov et al. 2001, 2003). The growth rate of a single ice dendrite is predicted by theoretical models of Langer and Müller-Krumbhaar (Langer 1980, 1989) with the assumption that the crystalline growth is exclusively driven by the thermal diffusion. At lower temperatures, the interface kinetics imposes additional limiting effects on phase change. The growth rate of a single ice dendrite in a sessile liquid film at $-10\ ^\circ$C, which is the lowest temperature of the SLD icing cloud, is approximately 0.03 m s^{-1} (Shibkov et al. 2001, 2003). However, experiments about the growth of free ice dendrites originating from a singular nucleation site in a stationary liquid do not replicate the situation of drop impact accurately, since with drop impact numerous initial nucleation sites could form simultaneously due to the impact and motion of the drop. Mechanical shock was identified as an effective trigger of nucleation in the work of Uhara et al. (1971) and Young (1911). In the presence of multiple initial nucleation sites, the growth of ice dendrites in the drop could complete more rapidly, and possibly influence the hydrodynamics of drop impact.

Studies on impact of a single supercooled water drop on solid surfaces were conducted often for the characterization of icing prevention or icing reduction properties of superhydrophobic surfaces (SHS) (Mishchenko et al. 2010; Wang et al. 2013). The SHS made of microstructured fluorinated silicone of Mishchenko et al. (2010) repelled supercooled water drops of $-5\ ^\circ$C completely with a tilt angle of $30°$ when the substrate was cooled to $-30\ ^\circ$C. In the case of normal impact, freezing occurred up to a substrate temperature of $-25\ ^\circ$C. The drop underwent a significant reduction in receding speed and decrease in maximum receding height as the substrate temperature further dropped. The delayed freezing of supercooled water on SHS was mainly attributed to surface chemistry, insulating properties of these surfaces, and increased free energy barrier to forming a critical ice nucleus at the liquid/solid interface (Alizadeh et al.

2012). Notable icephobic properties were demonstrated by PTES-coated surfaces of Wang et al. (2013), reducing the ice adhesion up to 87 % compared to that on a superhydrophilic surface. These PTES-coated surfaces possessed also remarkable durability by maintaining the functionality after 20 icing/ice-breaking cycles, presenting a good candidate for icephobic applications. Kulinich and Farzaneh (2009) found a correlation between the adhesion strength of glaze ice on hydrophobic surfaces to the contact angle hysteresis. More information on icephobic surfaces developed recently can be found in Bird et al. (2013) and Stone (2012). Numerical investigations on the impact of SLD also exist (Abdollahi et al. 2013).

Investigations of spray impact of supercooled water drops onto cold and warm surfaces of various wettability identified the effect of icing mitigation on SHS (Antonini et al. 2011; Kimura et al. 2007). In the experiment of Antonini et al. (2011), up to 80 % reduction in the heating power was observed for an electrical anti-icing system necessary to keep the heated leading edge of a wing free from icing. The runback water was significantly reduced or completely prevented, depending on the liquid water content of the spray cloud. These effects were attributed to drop shedding from the SHS due to drop rebound shortly after impact or due to aerodynamic drag (Antonini et al. 2011).

Although impact of supercooled water drops on solid surfaces and the accompanying solidification has been reported in the literature, the emergence of ice dendrites during a drop impact was not clearly observed in previous experiments.

In the following, we first introduce an experimental setup for generation of supercooled water drops and high-speed imaging of drop impact on both aluminum surfaces and superhydrophobic surfaces at controlled temperatures from 5 to $-20\ ^\circ$C. Formation of ice/water mixture resulting from the formation of ice dendrites was documented using both shadowgraph imaging and infrared imaging. The influence of solidification on drop spreading and drop receding was systematically investigated.

2 Experimental methods

2.1 Experimental setup

The experimental setup comprised a drop generator, a chilling tube for cooling of free falling drops, an experimental cell where the solid substrate was located, a high-speed camera for observation of the drop/wall collision, an LED illumination, and a data acquisition system. The main components of the experimental setup are shown schematically in Fig. 1.

Fig. 1 Schematic of the experimental setup. Single drops were created by a drop-on-demand pneumatic generator and fell through a chilling tube cooled by liquid nitrogen to become supercooled. The drop impacted onto a solid substrate in the experimental cell, and the event was recorded by a high-speed video camera with backlighting
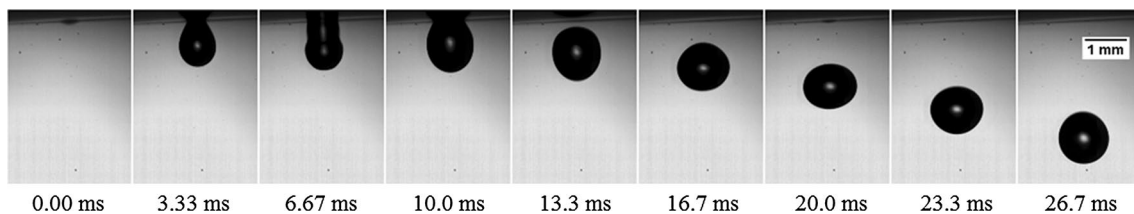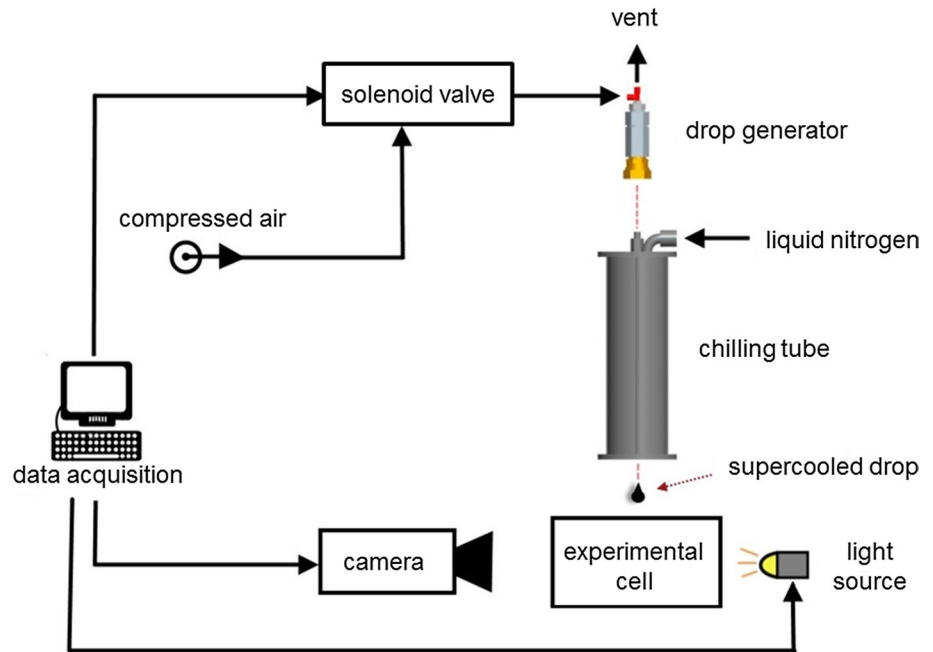
Fig. 2 Typical process of drop generation with the pneumatic drop-on-demand device

2.2 Drop generator

The operational principle of the drop generator is similar to the generator developed by Cheng and Chandra (2003). The core part of the drop generator is a small chamber consisting of a T-junction with exit tubes on the top, several thread adapters in the middle, an end cap, a Teflon sealing ring, and a pinhole at the bottom. The pinholes were optionally 500 or 800 μm in diameter, so that the maximum depth of the water in the small chamber was limited by the capillary action. A short pulse of pneumatic pressure was exerted onto the water of a small volume through one opening of the T-junction, and consequently a short liquid jet was squeezed through the pinhole at the bottom of the drop generator. The subsequent negative pressure resulting from the drainage of the gas from the other opening of the T-junction, which was connected to the atmosphere with an exit tube, pulled the water promptly back into the chamber, forming a neck at the pinhole between the ejected liquid and remaining liquid in the chamber.

With appropriate pressure settings and choices of T-junctions, drops in the diameter range 0.8–1.8 mm could be pinched off with nominally zero initial velocity, as shown in Fig. 2. The zero initial velocity of a drop was crucial to ensure a free fall without horizontal velocity components, which might lead to blockage of the chilling tube by drop impingement and rapid freezing of the deposited liquid.

The pressure level of the compressed air was controlled by a miniature pressure regulator (R308-P0, 0–0.25 bar, AirCom Pneumatic GmbH, Ratingen, Germany). The duration of the pulse was controlled by a solenoid valve (M 218 24 V = Landefeld, Germany) with the trigger signal provided by the NI 6602 digital counter module from a PC terminal. A commercial solid-state relay (100 kHz, MOS 5 V TTL/24VDC 0.1 A, Weidmüller, Germany) was applied to transform the digital 5 V signal from the NI 6602 module to the 24 V control signal to operate the solenoid valve. In order to observe the thin liquid film after drop impact, relatively big drops with a diameter of 1.6 ± 0.1 mm were used.

2.3 Drop cooling system

A 600-mm-long chilling passage was created by passing liquid nitrogen around a copper tube of 10 mm inner diameter. The drop fell through the chilling passage vertically within a short time of 500 ms. The final drop temperature at the exit of the chilling passage depends on the drop diameter and velocity.

In order to avoid condensation and to cool the drop generator to a temperature close to, but above 0 °C, the chilling tube and the drop generator were installed in a temperature-controlled enclosure.

The liquid nitrogen exiting from the chilling tube was warmed up and transformed to the gas phase in a compact heat exchanger with tap water flowing on the warm side. The dry nitrogen gas was then fed into the enclosure to surround the chilling tube and the drop generator, separating them from the air atmosphere. The temperature of the cold nitrogen gas was controlled at around −50 °C by varying the flow rates of the liquid nitrogen and the tap water.

A Peltier element with a power of 1.6 W and a surface temperature sensor (self-adhesive patch thermocouple, Conatex, St. Wendel, Germany) were glued to the brass end cap of the drop generator in order to prevent freezing of the water by heating on demand. The temperature of the brass end cap was kept at 0 °C in the experiment. Due to the thermal resistance of the end cap, the exact temperature of the water in the drop generator was not known exactly.

After falling through the chilling tube, the temperature of the drop varied from −3 to −5 °C, as measured by a high-speed infrared camera. It should be noted that only the surface temperature could be measured by infrared imaging; the interior of the drop was likely warmer. The velocity of the drop before collision on the substrate was 3.4 ± 0.1 m s^{-1}.

2.4 Substrates

Both hydrophilic and superhydrophobic surfaces were used for investigation of drop impact. The hydrophilic surface was a polished aluminum surface with an equilibrium contact angle of 40°. The roughness of the aluminum surface was 1.0 μm, measured by Mahr Perthometer (resolution 12 nm, Mahr GmbH, Göttingen, Germany). The SHS was produced by spray coating of aluminum surfaces with the liquid TEGOTOP (Evonik Degussa GmbH, Hanau, Germany). The equilibrium contact angle was measured as between 135° and 150°. This large variation of contact angle was possibly caused by inhomogeneous distribution of the solute in the TEGOTOP solution and imprecise control of the manual spray coating process. Another possible reason might be the various metastable configurations of drop/wall interface (Antonini et al. 2012; Li and Amirfazli 2005). The roll-off angle was measured to be between 28° and 32°. However, the main conclusions of the study will not be dependent on the exact value of contact angle, despite this variability. The surface roughness of the SHS was 4.5 μm, measured by INFINITEFOCUS (Alicona GmbH, Munich, Germany).

Condensation can effectively change the wettability of a solid surface (Bobinski et al. 2014; Xiao et al. 2008). In order to avoid condensation on the impact surface and to control the substrate temperature more precisely, an experimental cell was constructed to contain the impact surface in a closed space, as shown in Fig. 3. The only opening of the experimental cell was for the entry of supercooled water drops. Except for the short time of measurement, this opening was covered in order to prevent the buildup of humidity in the experimental cell.

The temperature of the impact surface was controlled precisely from 5 to −20 °C by a chilling machine
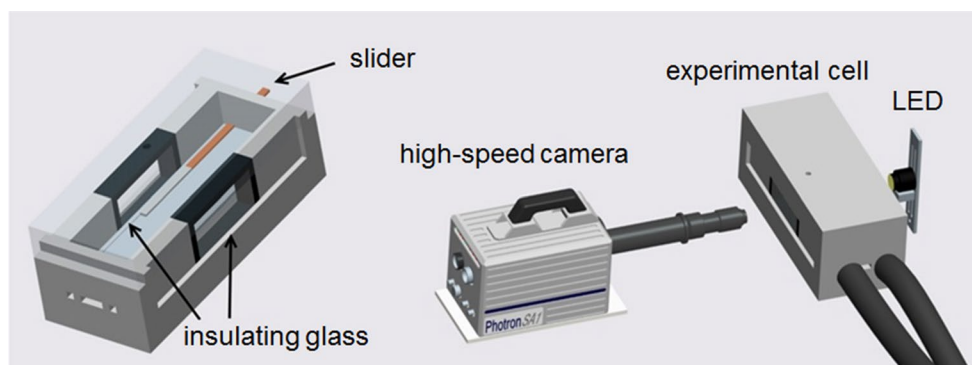
Fig. 3 Experimental cell (*left*) and the experimental configuration (*right*) for the shadowgraph imaging. The experimental cell was made of polystyrene with a thickness of 20 mm and a low thermal conductivity of 0.033 W m^{-2} K^{-1} for thermal insulation. The drop impacted onto the aluminum slider which lay in a slit in a chilling plate. The temperature of the chilling plate was regulated by internal circulating coolant. The optical access of the high-speed imaging system was provided by the insulating glass with a thermal conductivity of 3 W m^{-2} K^{-1}

(Unichiller UC020Tw, Peter Huber Kältemaschinenbau GmbH, Offenburg, Germany). When the air temperature in the experimental cell reduced below the dew point, condensation would not occur on the impact substrate, because it was about 1 °C warmer than the chilling plate due to the contact resistance between the aluminum slider and the chilling plate. Additionally a Peltier element of 41 W was glued on top of the cold plate by thermal paste, and an area of 40 mm × 40 mm was maintained at about −40 °C. Moisture would condense on this small area, lowering the relative humidity from saturation. At the lowest substrate temperature of −20 °C, total rebound of a drop on the SHS was observed, confirming that condensation on the solid substrate was effectively prevented.

2.5 Observation system

A Photron FASTCAM SA 1.1 was used for the high-speed imaging. A frame rate of 20 kHz was used, and the frame size was 768 (H) × 368 (V) with a spatial resolution of 13 µm pixel^{-1}, corresponding to a field of view of 9.98 mm (H) × 4.78 mm (V). The illumination was a customized LED lamp, which was composed of a high-power LED of 10 mm × 10 mm illuminating area glued onto a heat sink. A convex lens with a focal length of 20 mm and an aperture diameter of 20 mm was mounted in front of LED, in order to collimate the light beam.

2.6 Measurement of the drop temperature using the infrared camera

The experimental configuration of the infrared imaging was similar to the one shown in Fig. 3, except that the insulating glass on the camera side was replaced by an infrared window and that the illumination side was replaced with a polystyrene wall. The infrared window comprised two pieces of 4-mm-thick infrared glass of 40 mm diameter (NT63-215 Germanium Window, 8–12 µm, AR Coating, EdmundOptics) in a polystyrene wall. The structure of a double-glass window pane was for insulation, which avoided condensation on the outer surface of the infrared glass.

Infrared images were taken by "IRCAM Velox 327 k M" (IRCAM GmbH, Erlangen, Germany), a mid-wavelength infrared camera (MWIR) with the wavelength spectrum from 3.4 to 5 µm. The noise-equivalent temperature difference (NETD) of the mercury cadmium telluride (MCT) detector, which was cooled by a Stirling engine cryocooler, is 20 mK, providing sufficient precision for the intended temperature measurement. The infrared objective was "IR M 50" with a focal length 50 mm, an aperture of F/2, and an optimum wavelength spectrum from 3 to 5 µm. A custom-made extension ring of 10 mm width with black body coating was mounted between the objective and the

camera, in order to achieve a greater magnification. The resultant spatial resolution was 78 µm pixel^{-1}. The full frame had a pixel resolution of 640 × 512 with a dot pitch of 24 µm. The minimum pixel resolution of 256 × 256 was found to be sufficient for both the side-view and the bottom-view measurements, resulting in a field of view of 20 mm × 20 mm. The maximum frame rate at the minimum frame size was 820 Hz. However, only 718 Hz, with an integration time of 0.2 ms, was possible due to difficulties arising from the low temperatures applied in the experiment. According to the Stefan–Boltzmann law, the radiant emittance is proportional to the fourth power of the absolute temperature. As the temperature drops, the flux density of the thermal radiation decreases rapidly. Furthermore, Wien's displacement law says that the wavelength of the maximum radiation becomes larger as the temperature decreases. For the interested temperature range from 20 to −20 °C, the peaks lie between 8 and 12 µm, which do not coincide with the optimum spectrum of the camera detector and the infrared objective. At a faster frame rate, it was impossible to distinguish the drop from the background clearly.

Pixel-wise calibration of the infrared imaging was conducted from −20 to 20 °C in 1 °C steps using the experimental configuration with side-view infrared imaging. An aluminum plate with a frontal area of 40 mm × 40 mm coated with back body spray was placed in the slit of the chilling plate in order to provide a uniform temperature background. Since the heat transfer caused by the free convection in the experimental cell was negligible compared to the heat conduction, the temperature uniformity was adequate as examined by temperature measurement at different locations on the frontal surface of the aluminum plate with multiple surface temperature sensors. In the calibration, 100 images were recorded for an average at each temperature. The gray value of each pixel was related to the real temperature by a two-degree polynomial curve fitting, and the three coefficients of the parabolic function were saved in a three-layer TIF image. The standard derivation of the calculated temperature field with the calibration TIF data was below 0.2 °C, indicating the accuracy of the calibration.

Application of the infrared camera to the measurement of the temperature of the curved drop surface is not straightforward since this case differs from the calibration case in several aspects. If a surface is an ideal diffuse radiator, Lambert's cosine law says that the radiant intensity observed is directly proportional to the cosine of the angle θ between the observer's line of sight and the surface normal, as sketched in Fig. 4 (left). When the sensor element, dA, deviates from the normal direction of radiator surface element, dS, the radiant flux that dA receives from dS reduces according to Lambert's law. On the other hand, dA is able to "see" a larger area

Fig. 4 Lambert's cosine law (*left*; Haußecker 1996) and the directional emissivity, ε_β, of ice designated by curve "a" (*right*; Kabelac and Vortmeyer 2010)
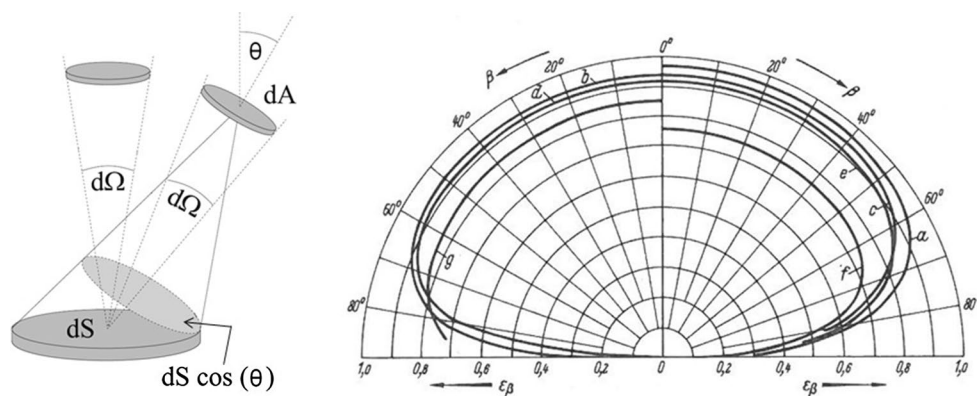
than dS. For a certain combination of detector and objective, the angular aperture is a fixed property of the imaging system. In Fig. 4 (left), the two solid lines originating from dA designate the angular aperture. Any surfaces lying between the two solid lines share the same projected area dS·cosθ, in the normal direction of dA. The projected area dS·cosθ is the area that dA perceives. For a Lambert's surface, all these surfaces send equal radiant flux to dA. In other words, the reduction in radiant flux according to the Lambert's law is exactly compensated by the enlargement of the visible area of the detector. Therefore, temperature measurement of a Lambert's surface, e.g., of a spherical shape, is the same as a flat surface parallel to the detector. Although water does not have exactly a Lambertian surface, the emissivity of water remains almost constant from the normal direction to the Brewster angle of about 50° (Haußecker 1996). Therefore, the central part of the drop surface can be approximated as Lambertian. The emissivity of ice is also orientation dependent as shown in Fig. 4 (right).

The second difference from the calibration case is caused by the dependency of the emissivity of water on the light wavelength (Robinson and Davies 1972). An average value for the entire wavelength spectrum of the interested range of temperature was chosen for the temperature measurement. This value was experimentally determined by the infrared imaging of a falling drop at known temperatures of 0 and 20 °C. The emissivity was found to be 0.97 in both cases.

The last source of the measurement error comes from reflection and transmission of the thermal radiation originating from the surrounding environment. The reflection coefficient is dependent on the refractive index and the angle of incidence, as known from the Fresnel equations. Although it is wavelength and temperature dependent, the refractive index for the limited wavelength spectrum of the imaging system, 3–5 μm, does not vary significantly in the interested temperature range from −20 to 5 °C, according to the data of Zasetsky et al. (2005) for water with and without supercooling. The refractive index was estimated

to be 1.2 for the experiment. With this value, it can be easily verified (Fresnel equations) that the reflection coefficient is 0.8 % for angles of incidence below the Brewster angle of 50°, deviating from the surface normal. The transmitted light ray is absorbed by water exponentially according to the Beer–Lambert Law. For the relevant range of the ambient temperature, the dominating wavelength spectrum is from 8 to 12 μm. Taking 10 μm for an estimate, the transmittance reaches 0 at a depth of 100 μm. Therefore, the temperature measurement is valid except at the marginal periphery of the drop. The central part of the drop has a reliable temperature measurement. This was confirmed by the infrared imaging of a drop at known temperatures.
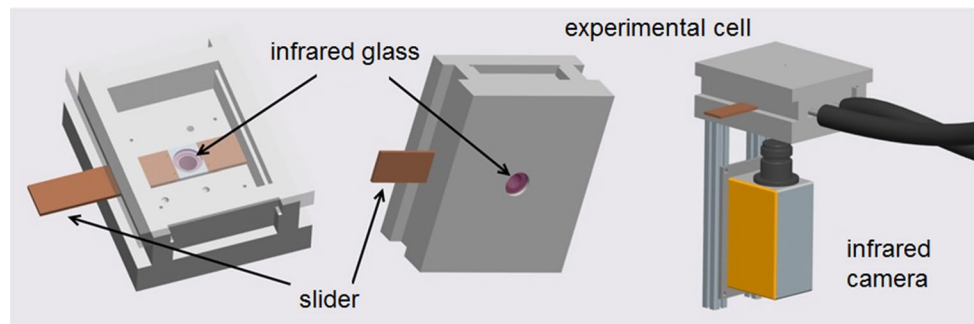
2.7 The bottom-view infrared imaging

A bottom-view infrared imaging was conducted to measure the temperature at the interface between the impacting drop and the substrate, as Fig. 5 illustrates. The drop impact took place on a 12-μm-thick aluminum film, which was placed on top of an infrared glass. The aluminum film provided a uniform temperature background and prevented drop impingement and icing directly on the infrared glass, which might damage the AR coating. The back side of the aluminum film had a black body coating in order to avoid reflection of the surrounding infrared radiation. The infrared glass and the aluminum film were cooled by a chilling plate underneath. The optical access was likewise provided by a double-glass infrared window pane. Table 1 lists the thermal properties of ice, aluminum, and the germanium infrared glass.

3 Results and discussion

3.1 Observations with shadowgraph imaging

Drop impact experiments were conducted on hydrophilic aluminum surfaces with a contact angle of 40°. The drops

Fig. 5 Experimental cell (*left*) and experimental configuration (*right*) for the bottom-view infrared imaging. The drop impacted onto an aluminum film on top of the infrared glass which was embedded in a

slider. The enclosure was made of polystyrene for thermal insulation. The optical access was provided by the infrared glasses. The chilling plate underneath the slider was cooled by internal circulating coolant

Table 1 Material properties of ice, aluminum, and germanium

	Ice at 0 °C	Aluminum	Germanium
k (W m^{-1} K^{-1})	2.22	237	60.2
ρ (kg m^{-3})	916	2700	5323
c_p (kJ kg^{-1} K^{-1})	2.05	0.897	0.3197
e (W s$^{1/2}$ K^{-1} m^{-2})	2.41×10^3	2.40×10^4	1.01×10^4

k thermal conductivity, ρ density, c_p specific heat capacity, $e = \sqrt{k\rho c_p}$ thermal effusivity

had three different initial (prior to impact) temperatures, 20, 0, and −4 °C with an uncertainty of about 1 °C. The substrate temperature varied from 0 to −20 °C. Figure 6 illustrates the typical phenomena observed. With either the drop temperature or the substrate temperature above 0 °C, both the spreading and the receding phases exhibited the same morphology as shown in Fig. 6 (left). The spreading and receding were symmetric, and the final deposited drop had a diameter smaller than the maximum spreading diameter.

When both the drop and the substrate temperatures were below 0 °C, the drop exhibited irregular sharp outlines during the spreading phase, and the periphery of the spreading drop frequently became pinned at the onset of the receding phase, as shown in Fig. 6 (right). This phenomenon probably indicates the inception of solidification during drop spreading.

The influence of solidification during drop impact was more apparent for superhydrophobic surfaces. With either the drop temperature or the substrate temperature above 0 °C, total rebound was observed as shown in Fig. 7. When both the drop and the substrate temperatures were below 0 °C, the drop exhibited an elongated contour (at 7.25 ms), a sharp edge (at 9.25 ms), or a cubic shape (at 64.75 ms), as shown in Fig. 8. Such shapes are impossible with a purely liquid drop, indicating that internal ice structures had

formed already before onset of the receding phase. Formation of such ice/water mixtures can only be caused by the rapid growth of ice dendrites. The emergence of the irregular shapes was observed to be random in time and location. Occasionally, zigzag drop contours appeared immediately upon impact.

It can be argued that the transition from total rebound to partial rebound was not due to the impalement (Bartolo et al. 2006; Reyssat et al. 2006), which is the transition of the liquid/solid contact from the Cassie–Baxter to Wenzel state. In the presence of sufficient impact force, impalement could occur and prevent total rebound (Antonini et al. 2013). Since total rebound was observed for impacts of warm drops above 0 °C onto substrates at all tested temperatures from 5 to −20 °C, the possibility of impalement is excluded. It is therefore inferred that partial solidification prevented the total rebound.

Figure 9 reveals the structure of the ice/water mixture formed during drop impact. The ice flake observed as a secondary drop has a similar structure to ice crystals formed in a stationary supercooled liquid (Langer 1980), further indicating that the ice/water mixture resulted from formation and growth of ice dendrites.

3.2 Observations with infrared imaging

Infrared imaging was applied to identify the rapid temperature rise of the drop during the growth of ice dendrites. As shown in Fig. 10, the drop warmed up from the initial −3 to 0 °C within 5.57–13.93 ms during drop rebound. Different from the ice dendrite in a sessile drop (Bauerecker et al. 2008; Jung et al. 2012) or that in a stationary liquid film (Shibkov et al. 2001, 2003), a clear ice dendrite front could not be observed. Instead, the drop temperature appeared spatially uniform, suggesting that nucleation sites occur throughout the entire drop. Despite the small variation of the initial drop

Fig. 6 Impact of a supercooled drop at −4 °C onto aluminum surfaces at 0 (*left*) and −10 °C (*right*). The drop diameters were 1.70 (*left*) and 1.73 mm (*right*). The impact velocities were 3.48 (*left*) and 3.56 m s^{-1} (*right*)
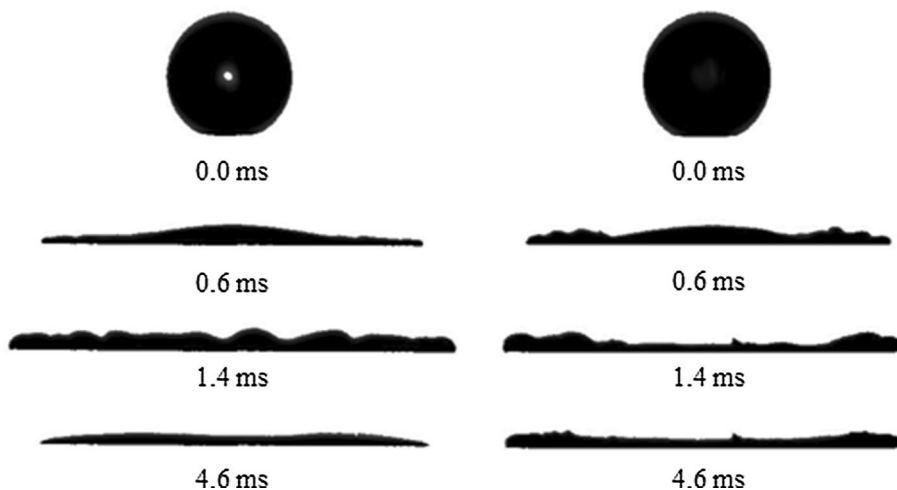
Fig. 7 Spreading, receding, and total rebound of a water drop with an initial temperature of 0 °C on a SHS at −10 °C. The drop diameter was 1.59 mm, and the impact velocity was 3.30 m s^{-1}. The *solid line* denotes the solid substrate. No irregular drop shapes were observed
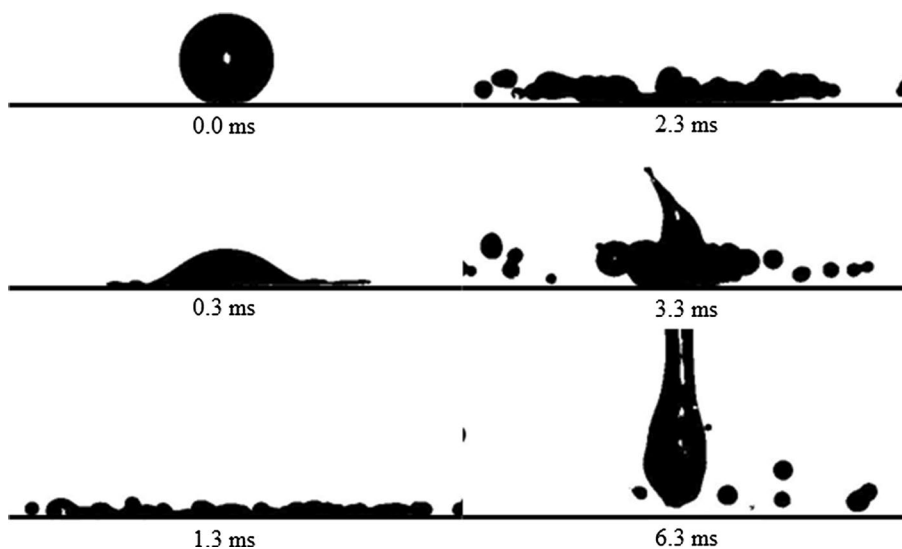
Fig. 8 Partial rebound of a supercooled drop at −4 °C on a SHS at 0 °C. The drop diameter was 1.57 mm, and the impact velocity was 3.38 m s^{-1}. The *solid horizontal line* marks the solid substrate. Some irregular drop shapes were observed, indicating at least partial solidification
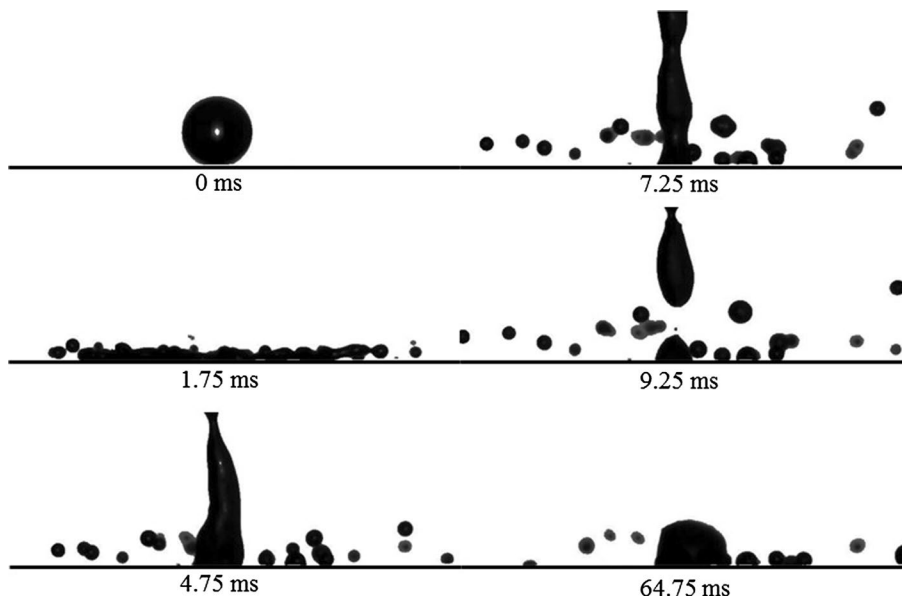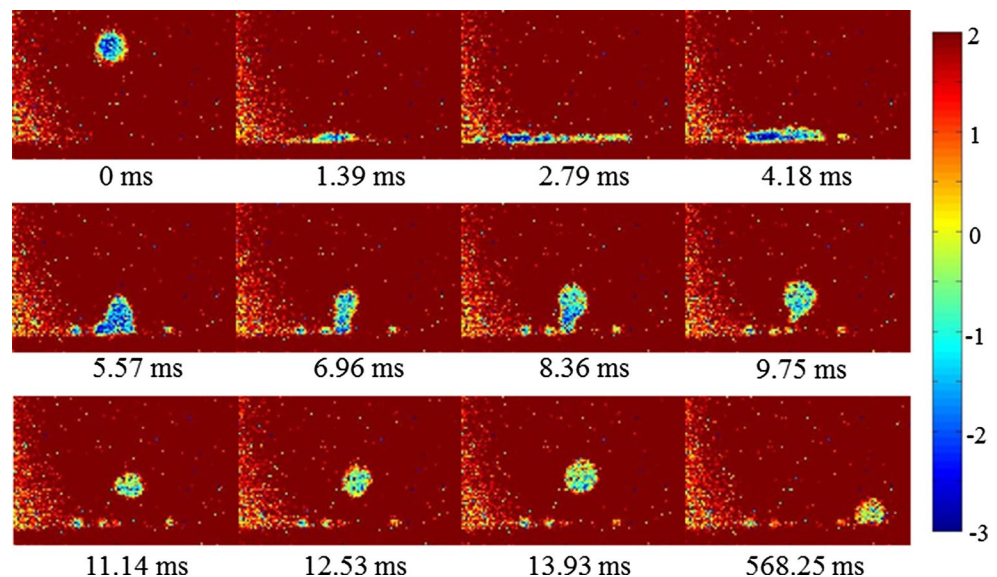
temperature from −3 to −5 °C, the duration of the temperature rise varied from 4.17 to 18.07 ms. The randomness is attributed to the uncontrollable formation of the initial nucleation sites (Toschev and Gutzow 1967; Bobinski et al. 2014).

The bottom-view infrared imaging provides a measurement of the interface temperature between the impinging drop and the solid substrate. Figure 11 represents typical measurement results at two substrate temperatures. The asymmetric decrease in the interface temperature on the −18 °C substrate indicates an irregular receding of the drop. The dry substrate quickly cooled back to the almost initial substrate temperature. On the substrate at −10 °C, the deposited drop exhibited an almost circular shape until the end of the recording.

Fig. 9 A secondary droplet with a composite structure of ice and water, which appeared during rebound of a supercooled drop on a SHS at 0 °C
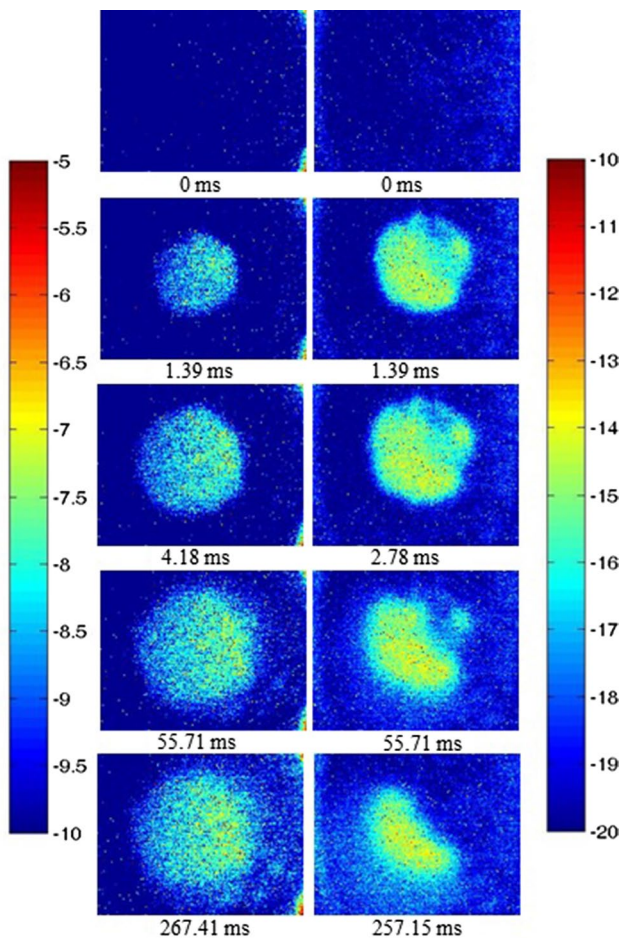
3.3 Influence of solidification on drop spreading

The transient spreading diameter was measured for drop impact on aluminum surfaces, as shown in Fig. 12. Four different cases referring to phase change were chosen: the impact of a 20 °C drop onto a 0 °C substrate without solidification, the impact of a 0 °C drop onto colder substrates with the slower stable solidification, the impact of a supercooled drop onto a 0 °C substrate with rapid formation and growth of ice dendrites, and the impact of a supercooled droplet onto colder substrates with both the growth of ice dendrites and the stable solidification.

The differences observed for supercooled droplets on the evolution of the drop spreading diameter are minor. The spreading at early times ($t^* \ll 1$) obeyed almost the square root law (Rioboo et al. 2002). One possible reason for the small influence of the subfreezing temperatures on drop spreading is the delay of solidification, which is especially long on superhydrophobic substrates (Toschev and Gutzow 1967; Boinovich et al. 2014). Even if the solidification is initiated at the early stages of drop impact, its effect will be negligibly small if the spreading velocity is higher than the solidification speed.

The measured maximum spreading diameters are shown in Fig. 13 in comparison with the theoretical model for isothermal drop impact (Roisman 2009). The comparison is, however, not straightforward, because the drop temperature continuously varies as it spreads on a substrate of a different temperature. As shown in Fig. 11, the drop/wall interface had a temperature close to the substrate temperature.

The interface temperature could be estimated by the contact temperature between two semi-infinite slabs as (Martin 2010),


Fig. 10 Infrared imaging of impact and total rebound of a supercooled drop with an initial temperature of −3 °C on a SHS at 5 °C. The substrate temperature was chosen to be well above 0 °C in order to ensure successful total rebound and to distinguish the drop from the ambient. A narrow temperature range was chosen for display in order to clearly exhibit the temperature rise. The image is cropped to 170 × 110 pixels with a field of view of 13.3 mm × 8.6 mm. The drop diameter was 1.5 mm, and the impact velocity was 3.4 m s⁻¹

Fig. 11 Measurement of the interface temperature between the impinging drop and the substrate. The drops were supercooled to -4 °C, the drop diameter was 1.6 mm, and the impact velocity was 3.4 m s^{-1}. The substrate temperatures were -10 (*left*) and -18 °C (*right*), respectively. The different temperature ranges for display (*left* and *right*) were intentionally chosen to clearly exhibit the temperature rise. The original images were cropped to 122×157 pixels for better illustration, corresponding to a field of view of 9.55 mm $\times$ 12.27 mm

$$T_K = \frac{T_{A-1} + \frac{e_2}{e_1} T_{A-2}}{1 + \frac{e_2}{e_1}}, \tag{1}$$

where T_K is the contact temperature, T_{A-1} and T_{A-2} denote, respectively, the initial temperatures of the two media, and e_1 and e_2 correspond to the thermal effusivities of the two media. Equation (1) holds only when the thermal boundary layer is much thinner than the height of the drop. A more comprehensive analysis of the heat transfer can be found in (Roisman 2010).

For the drop impact with supercooled water, the interface could be ice, supercooled water, water at 0 °C, or mixture of them: Eq. (1) is then not accurate. However, with ice
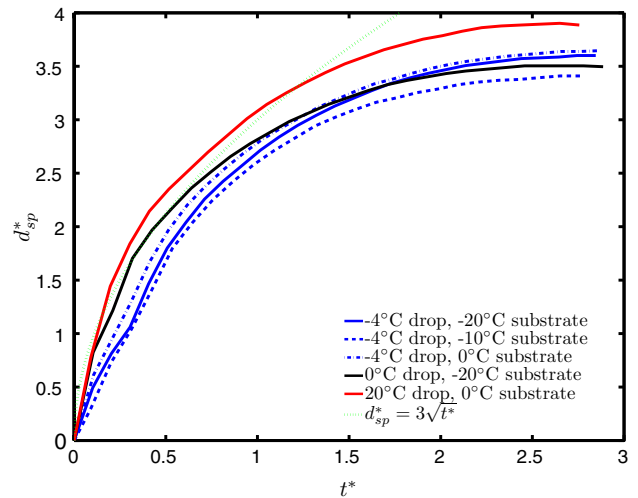
Fig. 12 Transient spreading diameter of the drop while impacting onto hydrophilic aluminum surfaces, measured from the instant of impact to the maximum spreading. The dimensionless spreading diameter is defined as $d_{sp}^* = d_{sp}/d_0$, where d_{sp} is the transient spreading diameter of the drop and d_0 is the initial diameter of the drop. The dimensionless time is defined as $t^* = t/\tau$, where the spreading time t is 0 at the instant of impact and $\tau = d_0/v_0$ is the time constant with v_0 designating the impact velocity. The polynomial curve fitting is based on the square root law (Rioboo et al. 2002)
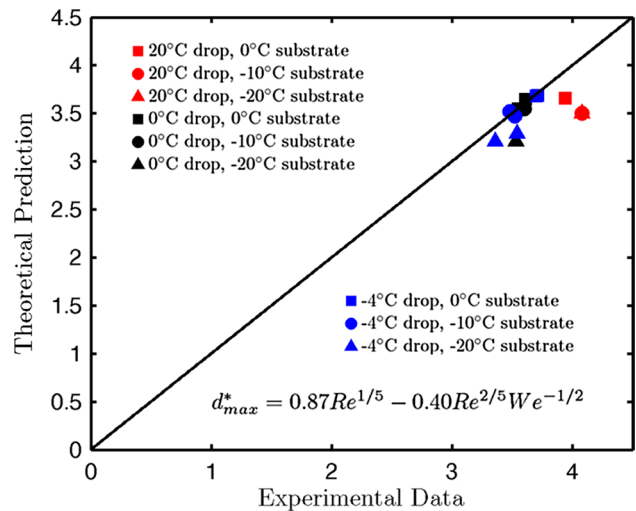
Fig. 13 Dimensionless maximum spreading diameter on hydrophilic aluminum surfaces. $d_{max}^* = d_{max}/d_0$, where d_{max} is the maximum spreading diameter and d_0 is the diameter of the impinging drop. The experimental data are compared with the theoretical model of Roisman (2009). The *We* and *Re* are calculated with the properties of water at the contact temperature T_K calculated according to Eq. (1). The two media in contact are water at the denoted temperatures and aluminum at the substrate temperatures. The density (Hare and Sorensen 1987), viscosity (Hallett 1963), surface tension (Holten et al. 2012), conductivity (Wagner and Kretzschmar 2010), and specific heat (Archer and Carter 2000) of supercooled water are taken at the corresponding temperatures

-4°C   -10°C   -20°C
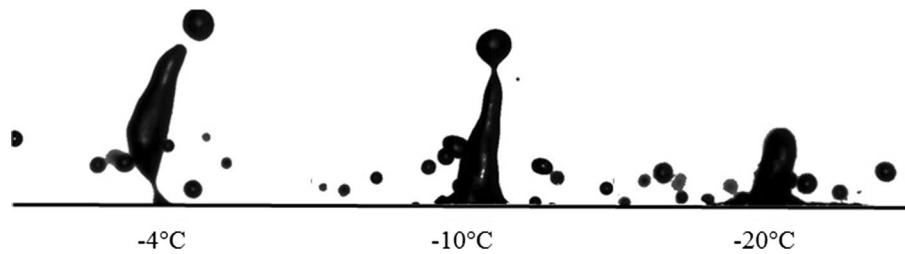
Fig. 14 Influence of the substrate temperature on the receding of supercooled water drops on SHSs. The substrate temperature is given below the image. The solid line denotes the impact surface. The images were taken at the instant of the minimum receding diameter. The diameters of the impinging drop were approximately 1.6 mm, and the impact velocities were around 3.4 m s^{-1}

at 0 °C and germanium at -10 and -18 °C for the two contacting media, Eq. (1) yields -8 and -15 °C, respectively, values which are in good agreement with the measured values of -7.5 ± 0.5 and -14.5 ± 0.5 °C in the bottom-view infrared imaging as shown in Fig. 11. On aluminum surfaces, the contact temperature is closer to the initial temperature of the substrate on account of higher thermal effusivity of aluminum than of germanium.

Since velocity and diameter of the drop were almost constant, *We* and *Re* of the drop impact were mainly dependent on the liquid properties which vary with the drop temperature. With the liquid properties at the initial temperatures of the drop, *We* and *Re* ranged from 200 to 300 and from 2600 to 5800, respectively. Since the drop cools down during spreading, liquid properties at the contact temperature are chosen for the theoretical prediction. The model of Roisman agrees well with the experimental data when the temperature difference between the drop and the substrate was <10 °C, as shown in Fig. 13. With larger temperature differences between the drop and the substrate, the theoretical predictions were smaller than the experimental data. This discrepancy results from difficulties in the determination of liquid properties. Therefore, it is further indicated that the influence of solidification on drop spreading was minor.

3.4 Influence of solidification on drop receding

The impact of supercooled drops was conducted on a SHS of decreasing temperature, from 0 to -20 °C. The drop rebound remained uninfluenced until the substrate temperature decreased to -2 °C. At lower substrate temperatures, the central part of the drop appeared to be frozen on the solid surface and consequently prevented total rebound. The residual frozen area became larger as the substrate temperature dropped, as shown in Fig. 14. The pictures are selected at the instant when the drop/wall interface reached a minimum diameter during the receding phase, which is designated as the minimum receding diameter d_{min}.

Wang et al. (2013) observed total rebound of water drops at -10 °C on aluminum-based SHSs warmer than -10 °C,

a lower substrate temperature than in our experiment. The impact velocity in the experiment of Wang et al. was up to 0.99 m s^{-1}. The mechanical shock brought by the drop impact could be insufficient to trigger the nucleation (Uhara et al. 1971). With the same impact velocity of 3.4 m s^{-1}, solidification might also occur to the SHSs of Wang et al.

In the experiment of Mishchenko et al. (2010), total rebound of -5 °C drop was observed on silicon-based SHSs at an even lower temperature, -25 °C. The impact velocity with a 10 cm falling distance was about 1.4 m s^{-1}. This effect is possibly brought by the thermal properties of the solid substrate. Silicon has a lower thermal effusivity (1.59×10^4 W s$^{1/2}$ K^{-1} m^{-2}) than aluminum (2.40×10^4 W s$^{1/2}$ K^{-1} m^{-2}). The height of the microstructures of the silicon-based SHS, from 7.5 to 10.9 µm, was higher than the surface roughness of 4.5 µm in the experiments of Wang et al. and ours. As a result, the temperature of the drop/wall interface was probably higher on the silicon-based SHS of Mishchenko et al. than on the aluminum-based SHS at equal substrate temperatures.

Figure 15 quantifies the relationship between the minimum receding diameter, d_{min}, and the substrate temperature, T_S. Since the drop diameter and the impact velocity were limited to a narrow range, T_S was the only independent variable in this analysis. d_{min}^* was found to change almost linear with T_S until -12 °C and leveled off when T_S dropped below -15 °C. The data scatter could be attributed to the randomness in the formation of initial nucleation sites and the irregular influence of ice dendrites on the drop deformation. The final deposited drop on the substrate had irregular shapes.

The minimum receding diameter indicates the coverage of ice on the substrate. The speeds of ice accretion on substrates are also plotted in Fig. 15 in comparison with the growth rates of free ice dendrites at the corresponding temperatures. It is found that the speed of ice accretion on the substrate is faster than the growth rate of ice dendrites in sessile drops. It is possible that multiple nucleation sites formed during drop spreading and that ice dendrites grew simultaneously throughout different portions of the drop.
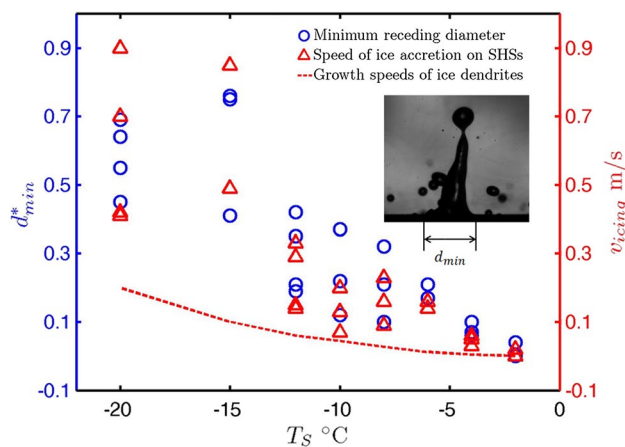
Fig. 15 Dimensionless minimum receding diameter and the speed of ice accretion resulting from impact of supercooled water drops at $-4\,^{\circ}C$ on SHS substrates from 0 to $-20\,^{\circ}C$. The dimensionless minimum receding diameter is scaled by the maximum spreading diameter as $d^*_{\min} = d_{\min}/d_{\max}$. $d_{\max}$ was measured before the periphery of the flattened drop separated in the form of secondary droplets. The speed of ice accretion on SHSs is defined as $v_{\text{icing}} = d_{\min}/2t_{\text{contact}}$, where t_{contact} is the icing time measured from the instant of impact to the instant when $d_{\min}$ was reached. The growth speeds of ice dendrites are taken from Shibkov et al. (2003). The diameters of the impinging drop were approximately 1.6 mm, and the impact velocities were around 3.4 m s^{-1}

4 Conclusions

Single drop impact of supercooled water at $-4 \pm 1\,^{\circ}C$ onto hydrophilic and superhydrophobic surfaces at temperatures from 5 to $-20\,^{\circ}C$ with an impact velocity of approximately 3.4 m s^{-1} was investigated experimentally.

The transient spreading diameter and the maximum spreading diameter were measured. Both parameters remained uninfluenced by temperature despite the emergence of the ice structures during drop spreading. The reason is attributed to the possible solidification delay or the slower solidification speed compared to the spreading velocity. The maximum spreading diameter was adequately predicted by a theoretical model developed for isothermal drop impact without consideration of the phase change, indicating that the spreading phase remains inertially dominated. Receding of the deposited drop was found to be asymmetric when both the drop and substrate temperatures were below 0 °C, clearly indicating partial solidification on the substrate.

The outcomes of the drop impact onto superhydrophobic surfaces were strongly dependent on the initial temperatures of the drop and the substrate. With a supercooled drop and a substrate below the freezing point, the rapid formation of ice dendrites led to freezing of the drop on the substrate. The dimensionless minimum receding diameter, which indicates the residual iced area, was found to scale almost linearly with the substrate temperature above $-12\,^{\circ}C$, but was basically constant at lower substrate temperatures. The speed of ice accretion on the substrate in the dynamic process of drop impact was significantly higher than the growth rate of free ice dendrites in sessile liquids, indicating multiple nucleation sites subsequent to impact.

References

Abdollahi V, Habashi W, Fossati M, Baruzzi G (2013) Quasi-molecular modeling of supercooled large droplets dynamics for in-flight icing simulations. In: At the 5th AIAA atmospheric and space environment conferences. San Diego. AIAA 2013-3057

Alizadeh A et al (2012) Dynamics of ice nucleation on water repellent surfaces. Langmuir 28:3180–3186

Antonini C, Amirfazli A, Marengo M (2012) Drop impact and wettability: from hydrophilic to superhydrophobic surfaces. Phys Fluids 24:102104

Antonini C et al (2011) Understanding the effect of superhydrophobic coatings on energy reduction in anti-icing systems. Cold Reg Sci Technol 67:58–67

Antonini C et al (2013) Drop rebound after impact: the role of the receding contact angle. Langmuir 29:16045–16050

Archer DG, Carter RW (2000) Thermodynamic properties of the NaCl + H$_2$O system. 4. Heat capacities of H$_2$O and NaCl(aq) in cold-stable and supercooled states. J Phys Chem B 104(35):8563–8584

Bartolo D et al (2006) Bouncing or sticky droplets: impalement transitions on superhydrophobic micropatterned surfaces. Europhys Lett 74:299–305

Bauerecker S et al. (2008) Monitoring ice nucleation in pure and salty water via high-speed imaging and computer simulations. J Phys Chem C 112(20):7631–7636

Bernstein BC, Ratvasky TP, Miller DR, McDonough F (1999) Freezing rain as an in-flight icing hazard. In: 8th conference on aviation, range and aerospace meteorology, January 10–15. American Meteorological Society, Dallas, Texas. NASA/TM-2000-210058

Bird JC, Dhiman R, Kwon H-M, Varanasi KK (2013) Reducing the contact time of a bouncing drop. Nature 503:385–388

Bobinski T et al (2014) Droplet impact in icing conditions—the influence of ambient air humidity. Arch Mech 66(2):127–142

Boinovich L, Emelyanenko A, Korolev V, Pashinin A (2014) Effect of wettability on sessile drop freezing: when superhydrophobicity stimulates an extreme freezing delay. Langmuir 30(6):1659–1668

Cheng S, Chandra S (2003) A pneumatic droplet-on-demand generator. Exp Fluids 34:755–762

Cober SG, Isaac GA (2006) Estimating Maximum aircraft icing environments using a large data base of in situ observations. In: 44th AIAA aerospace sciences meeting and exhibit. Reno, Nevada. AIAA 2006-266

Cober SG, Isaac GA, Strapp JW (2001) Characterizations of aircraft icing environments that include supercooled large drops. J Appl Meteorol 40(11):1984–2002

Hallett J (1963) The temperature dependence of the viscosity of supercooled water. Proc Phys Soc 82(6):1046

Hare DE, Sorensen CM (1987) The density of supercooled water II. Bulk samples cooled to the homogeneous nucleation limit. J Chem Phys 87(8):4840–4845

Haußecker H (1996) Messung und simulation von kleinskaligen austauschvorgängen an der ozeanoberfläche mittels thermographie, Dissertation, Ruprecht-Karls-Universität Heidelberg, Germany

Holten V, Bertrand CE, Anisimov MA, Sengers JV (2012) Thermodynamics of supercooled water. J Chem Phys 136:094507. doi:10.1063/1.3690497

Jung S, Tiwari MK, Vuong Doan N, Poulikakos D (2012) Mechanism of supercooled droplet freezing on surfaces. Nat Commun 3:615. doi:10.1038/ncomms1630

Kabelac S, Vortmeyer D (2010) K1 radiation of surfaces. In: VDI-GVC (ed) VDI heat atlas, 2nd edn. Springer, Düsseldorf, Germany, p 949

Kimura S et al. (2007) A new surface coating for prevention of icing on airfoils. In: Proceedings of SAE aircraft and engine icing international conference. Seville, Spain

Kulinich SA, Farzaneh M (2009) How wetting hysteresis influences ice adhesion strength on superhydrophobic surfaces. Langmuir 25(16):8854–8856

Langer JS (1980) Instabilities and pattern formation in crystal growth. Rev Modern Phys 52:1

Langer JS (1989) Dentrites, viscous fingers, and the theory of pattern formation. Science 243:1150–1156

Li W, Amirfazli A (2005) A thermodynamic approach for determining the contact angle hysteresis for superhydrophobic surfaces. J Colloid Interface Sci 292:195–201

Martin H (2010) E2 transient conduction in stagnant media. In: VDI-GVC (ed) VDI heat atlas, 2nd edn. Springer, Düsseldorf, Germany, pp 647–648

Marwitz JD et al (1997) Meteorological conditions associated with the ATR-72 aircraft accident near Roselawn, Indiana on 31 October 1994. Bull Am Meteorol Soc 78(1):41–52

Mingione G, Iuliano E, Guffond D, Tropea C (2011) EXTICE: EXTreme icing environement. SAE technical paper 2011-38-0063

Mishchenko L et al (2010) Design of ice-free nanostructured surfaces based on repulsion of impacting water droplets. ACS Nano 4(12):7699–7707

Mullins WW, Sekerka RF (1963) Morphological stability of a particle growing by diffusion or heat flow. J Appl Phys 34(2):323–329

Mullins WW, Sekerka RF (1964) Stability of a planar interface during solidification of a dilute binary alloy. J Appl Phys 35(2):444–451

Reyssat M et al (2006) Bouncing transitions on microtextured materials. Europhys Lett 74:306–312

Rioboo R, Marengo M, Tropea C (2002) Time evolution of liquid drop impact onto solid. Dry Surf Exp Fluids 33:112–124

Robinson PJ, Davies JA (1972) Laboratory determinations of water surface emissivity. J Appl Meteorol 11:1391–1393

Roisman IV (2009) Inertia dominated drop collisions II. An analytical solution of the Navier-stokes equations for a spreading viscous film. Phys Fluids 21:052104. doi:10.1063/1.3129283

Roisman IV (2010) Fast forced liquid film spreading on a substrate: flow, heat transfer and phase transition. J Fluid Mech 656:189–204

Shibkov AA et al. (2001) Kinetics and morphology of nonequilibrium growth of ice in supercooled water. Crystallogr Rep 46(3):496–502

Shibkov AA et al. (2003) Morphology diagram of nonequilibrium patterns of ice crystals growing in supercooled water. Phys A 319:65–79

Stone HA (2012) Ice-phobic surfaces that are wet. ACS Nano 6(8):6536–6540

Strapp JW, Stuart RA, Isaac GA (1996) A Canadian climatology of freezing precipitation and a detailed study using data from St. John's, Newfoundland. In: Proceedings of FAA international conference on aircraft inflight icing, 6–8 May 1996. Springfield, Virginia, pp 45–66

Toschev S, Gutzow I (1967) Time lag in heterogeneous nucleation. Phys Stat Sol B 21:683

Uhara I, Doi S, Makino M, Teratani S (1971) Crystal nucleation given rise by fracturing or by mechanical shock. Kolloid-Zeitschrift und Zeitschrift für Polymere 244:218–222

Wang Y et al (2013) Verification of icephobic/anti-icing properties of a superhydrophobic surface. ACS Appl Mater Interfaces 5:3370–3381

Wagner W, Kretzschmar H-J (2010) D2.1 properties of water and steam. In: VDI-GVC (ed) VDI heat atlas, 2nd edn. Springer, Düsseldorf, Germany, p 154

Xiao X, Cheng Y-T, Sheldon BW, Rankin J (2008) Condensed water on superhydrophobic carbon films. J Mater Res 23:2174–2178

Young SW (1911) Mechanical stimulus to crystallization in supercooled liquids. J Am Chem Soc 33:148–162

Zasetsky AY, Khalizov AF, Earle ME, Sloan JJ (2005) Frequency dependent complex refractive indices of supercooled liquid water and ice determined from aerosol extinction spectra. J Phys Chem A 2005(109):2760–2764